JET–P(99)44

L C Ingesson

Limitations to Total Radiated Power Determination in Divertor Tokamaks

JET–P(99)44

Limitations to Total Radiated Power Determination in Divertor Tokamaks

L C Ingesson.

JET Joint Undertaking, Abingdon, Oxfordshire, OX14 3EA,

Preprint of a Paper to be submitted for publication in Review of Scientific Instruments

November 1999

ABSTRACT

The electromagnetic total power radiated from the plasma in a tokamak is often estimated by a weighted summation of some bolometer channels. Although this method may be reliable for limiter plasmas, theoretical considerations and a comparison with total radiated powers determined from tomographic reconstructions show that for diverted plasmas with much radiation from the divertor region such estimates can be unreliable, unless the used lines of sight are parallel. The sparseness of the sampling, however, has little effect on the total radiated power calculation if the beam widths are similar to the distance between lines of sight.

PACS numbers: 52.70.Kz, 52.25.Qt, 52.55.Fa

1. INTRODUCTION

The total radiated power in tokamaks is an important plasma parameter that is required routinely during operations and in the analysis of discharges. The total radiated power can be estimated in various ways, ranging from a simple weighted summation of bolometer lines of sight that can be calculated between discharges, to an elaborate tomographic reconstruction that requires input by hand and can only be carried out for a limited number of time slices in a limited number of discharges.

The theory and application of the weighted summation technique is discussed Sec. 3. The technique is illustrated for the bolometer system of the JET (Joint European Torus) tokamak with simulated and measured data, introduced in Sec. 2. In addition, the effects on the calculated total radiated power due to the finite width of the instrument functions (beam width) are studied in Sec. 4.

2. JET BOLOMETERS, PLASMA EMISSION AND TOMOGRAPHY

At JET, the vertical camera of the old three-camera bolometer system[1,2] (called KB1, see Fig. 1 for the lines of sight) is used for the approximate total radiated power calculation by weighted summation. This system can also be used for tomographic reconstructions; however, to obtain more accurate reconstructions and to resolve more detail in the divertor, typically 45 newer bolometer channels are available.[3,4] The bolometer systems are located in different octants of the tokamak; toroidal asymmetry of the emissivity has to be assumed to make tomographic reconstructions in one poloidal cross-section and to obtain a good estimate of the total radiated power. The bolometer systems also detect neutral particles produced in the plasma by charge-exchange processes.[5,6] The contribution from neutral particles is mainly relevant for the study of the power balance in the divertor and is outside the scope of the present paper, which is concerned only with the electromagnetic loss power. The KB1 cameras are pin-hole cameras, i.e. all channels of one camera view through one aperture. The positions of the detectors and sizes of the apertures were chosen such as to obtain a good coverage of the plasma (Fig. 1) without gaps

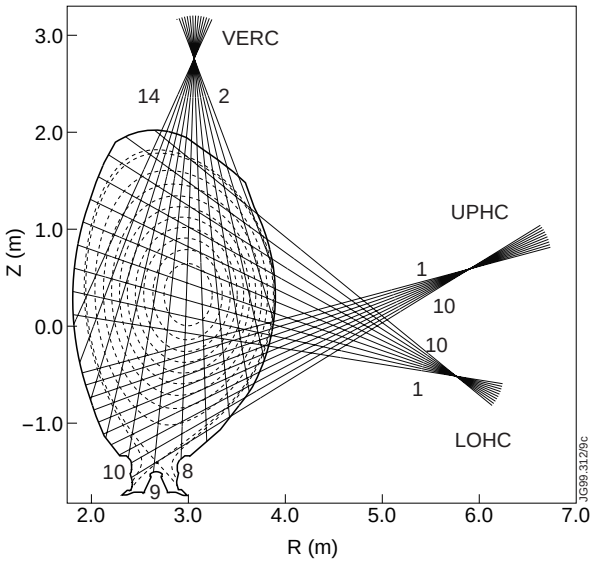

Fig.1: Lines of sight of the three cameras of the KB1 bolometer system with respect to a poloidal cross-section of the inner wall of the JET vacuum vessel. The dotted curves indicate typical magnetic flux surfaces.

between the viewing beams (see also Sec. 4). The latter property is also beneficial to maximize the signal-to-noise ratio by maximizing the amount of light received without loss of information.

Diverted plasmas are characterized by a significant amount of radiation from the divertor. Although the divertor volume is much smaller than the volume of the bulk plasma (about 4%), as much as half of the radiated power can be radiated from the divertor. The divertor radiation profile is typically very peaked at the strike points during attached operation (low density), and peaked near the X point during detached operation (high density). Figure 2(a) shows the emissivity (mainly radiated by carbon impurities) in the divertor region in the attached phase of a L-mode plasma simulated by two-dimensional transport code EDGE2D/NIMBUS (see Ref. 6 for a more detailed description of these particular simulations). The sparse and irregular coverage of the plasma [Fig. 2(b)] and the very localized and peaked emission in the divertor make tomographic reconstructions of the bolometer measurements difficult. The most successful tomographic reconstruction algorithm used for bolometry at JET is a constrained-optimization method that uses smoothness as object function and the discrepancy principle as constraint.[5,7] For best results it is necessary to include the finite width of the viewing beams and to use a non-negativity constraint,[5,8] as has been done in Figs. 2(c)–2(e). Figure 2(c) shows a tomographic reconstruction of the simulated bolometer measurements, i.e. what would be measured if Fig. 2(a) were the actual emission profile. The reconstruction is not particularly good: it indicates that it is impossible to resolve details of the plasma emission from the available lines of sight [Fig. 2(b)]. It should be said that usually better reconstructions are obtained for detached plasmas with more radiation near the X point and less at the targets.[6,8] This example of an attached plasma was chosen because it is more difficult to determine the total radiated power and can be considered to be a worst-case scenario. Figure 2(d) shows the tomographic reconstruction with simulated KB1 data only, and Fig. 2(e) is the reconstruction with all available channels for actual measurements.

Tomographic reconstruction is the determination of the emission profile $g(R,Z)$, where R is the major radius and Z the height above the midplane (i.e. Cartesian coordinates of a poloidal cross-section), from line-integral or beam-integral measurements. Line-integral measurements are given by

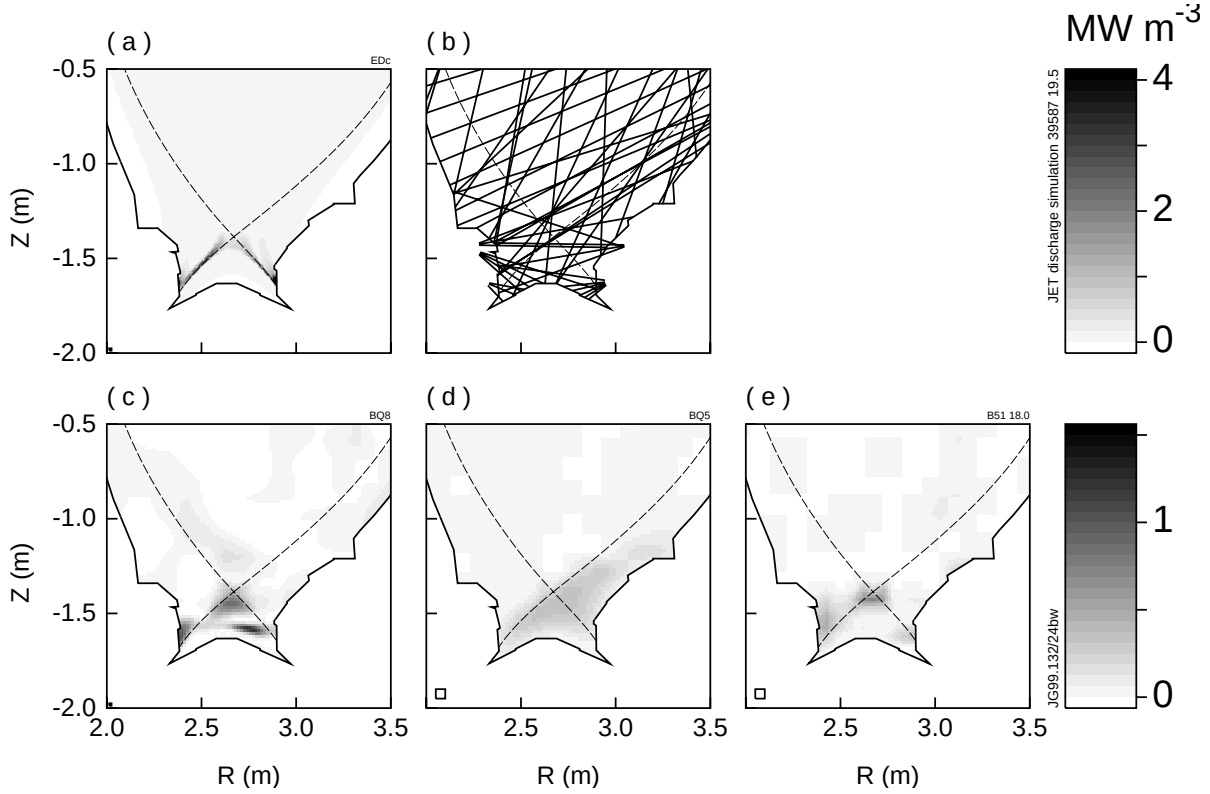

Fig.2: (a) The radiation profile of an attached divertor plasma predicted by a two-dimensional transport code simulation. (b) Lines of sight of all JET bolometers systems in the divertor region used in the reconstructions. (c,d) Tomographic reconstructions of simulated bolometer measurements, i.e. calculated from the emission profile (a), using all available lines of sight (c) and KB1 only (d). (e) Tomographic reconstruction of actual measurements of the discharge simulated. The box in the lower-left corner indicates the grid size in the divertor, the dashed curve the separatrix of the plasma. The reconstructions with all lines of sight have been shown not to depend on the grid size [whether it is as large as in (d) or as small as in (c)], as long as the grid size is smaller than the average distance between lines of sight.[8]

$$f(p,\xi) = \iint g(R,Z)\,\delta(p + (R-R_0)\sin\xi - (Z-Z_0)\cos\xi)\,\mathrm{d}R\,\mathrm{d}Z\,, \qquad (1)$$

where (R_0, Z_0) is a chosen origin, for example the magnetic axis, and (p,ξ) parametrize a line of sight and are coordinates of projection space: p is the signed distance from the origin to the line and ξ is the angle of the line with the positive R axis. Tomographic reconstruction is the inversion of Eq. (1). The image $f(p,\xi)$ for a given emission profile $g(R,Z)$, i.e. values $f(p,\xi)$ for (p,ξ) on a regular grid, is called the sinogram of $g(R,Z)$. The range of (p,ξ) is usually chosen as follows: $-a \le p \le a$, where a is the maximum distance from the origin (R_0, Z_0) for which $g(R,Z)$ is nonzero, and $0 \le \xi < \pi$.

In reality the measurements are not along infinitely thin lines and an instrument function has to be taken into account. If the detectors of one camera share a pin hole, if the apertures and detectors are small compared with the dimensions of the plasma and the beam widths, and if the geometry of the channels of that camera is approximately equal (i.e. shift-invariant instrument functions), it is convenient to describe the measurement as a convolution of the sinogram values on the aperture curve with the instrument function. If the common aperture has coordinates $(R_{\mathrm{ap}}, Z_{\mathrm{ap}})$, the aperture curve in projection space is given by [Fig. 3(b)]

$$p_{\mathrm{ap}}(\xi) = -(R_{\mathrm{ap}} - R_0)\sin\xi + (Z_{\mathrm{ap}} - Z_0)\cos\xi .$$

The instrument function in this case is called angular étendue $e(\xi)$.[9] Normally this quantity has dimensions $\mathrm{rad\,m^2}$, but here it will be normalized such that $\int e(\xi)\,\mathrm{d}\xi = 1$. The convolution that describes the measurements $\hat{f}(p,\xi)$ that are blurred by the instrument function is

$$\hat{f}(p_{\mathrm{ap}}(\xi),\xi) = \int_0^{\pi} e(\xi' - \xi)\, f(p_{\mathrm{ap}}(\xi'),\xi')\,\mathrm{d}\xi' . \tag{2}$$

Note that because of the normalization of $e(\xi)$ the units and scaling of $\hat{f}(p,\xi)$ and $f(p,\xi)$ is the same. The total radiated power can be determined from the emission profiles in one poloidal cross-section. Assuming toroidal symmetry, the total radiated power is the toroidal volume integral

$$P = 2\pi \iint g(R,Z)\, R\,\mathrm{d}R\,\mathrm{d}Z . \tag{3}$$

The total radiated powers obtained in this way from the simulation [Figs. 2(a)] and the tomographic reconstructions of Figs. 2(c) and 2(d) are given in Table I. The values obtained depend little on variations in reconstruction parameters; a more detailed discussion on the influence of reconstruction parameters can be found in Ref. 8.

3. WEIGHTED SUMMATION

3.1 Background

The area integral

$$\tilde{P} = \iint g(R,Z)\,\mathrm{d}R\,\mathrm{d}Z = \int f(p,\xi)\,\mathrm{d}p \tag{4}$$

is independent of angle ξ: all vertical integrals of the sinogram are equal. Relating Eq. (4) to the toroidal volume integral of Eq. (3), one can write

$$P = 2\pi \int f(R,\xi = \pi/2)\, R\,\mathrm{d}R \approx 2\pi R_0 \tilde{P}, \tag{5}$$

where R has been identified with p for $\xi = \pi/2$. For a machine with the aspect ratio of JET, the approximation with the constant R_0 is not bad: it only deviates some per cent from the proper integral over R. The consequence of Eqs. (4) and (5) is that if measurements exist on or can be mapped to any $\xi = \mathrm{const}$ line, a reasonable approximation of the total radiated power can be obtained from the integral along this line. Provided parallel lines of sight or an accurate mapping to parallel lines of sight are available, this procedure is highly preferable to calculating the total radiated power from a tomographic reconstruction as it is a robust integral method, whereas the tomographic reconstruction is a noise-sensitive differential operation (ill-posed problem).

Discretization of Eq. (5) gives

$$P \approx 2\pi R_0 \sum\nolimits_i f(p_i, \xi = \mathrm{const})\,\Delta p_i . \tag{6}$$

Equation (6) will be referred to as the weighed-summation method to determine the total radiated power, the weights being given by Δp_i between the discrete measurements. If measurements existed along a line $\xi = \text{const}$ (i.e. parallel lines of sight covering the entire cross-section), only discretization errors and an error due to constant R_0 would be made with this method. In reality, however, no such measurements exist on JET and many other tokamaks [Fig. 3(a)]. The set of measurements closest to $\xi = \text{const}$ is the vertical camera, of which the aperture curve and average location of the measurements are shown in Fig. 3(b). The main problem in applying the weighted summation method to JET data (and data from other tokamaks) is that an accurate mapping from the aperture curve to a $\xi = \text{const}$ line has to be found. Two ways of doing this are indicated in Figs. 3(b)–3(e) and will be discussed next.

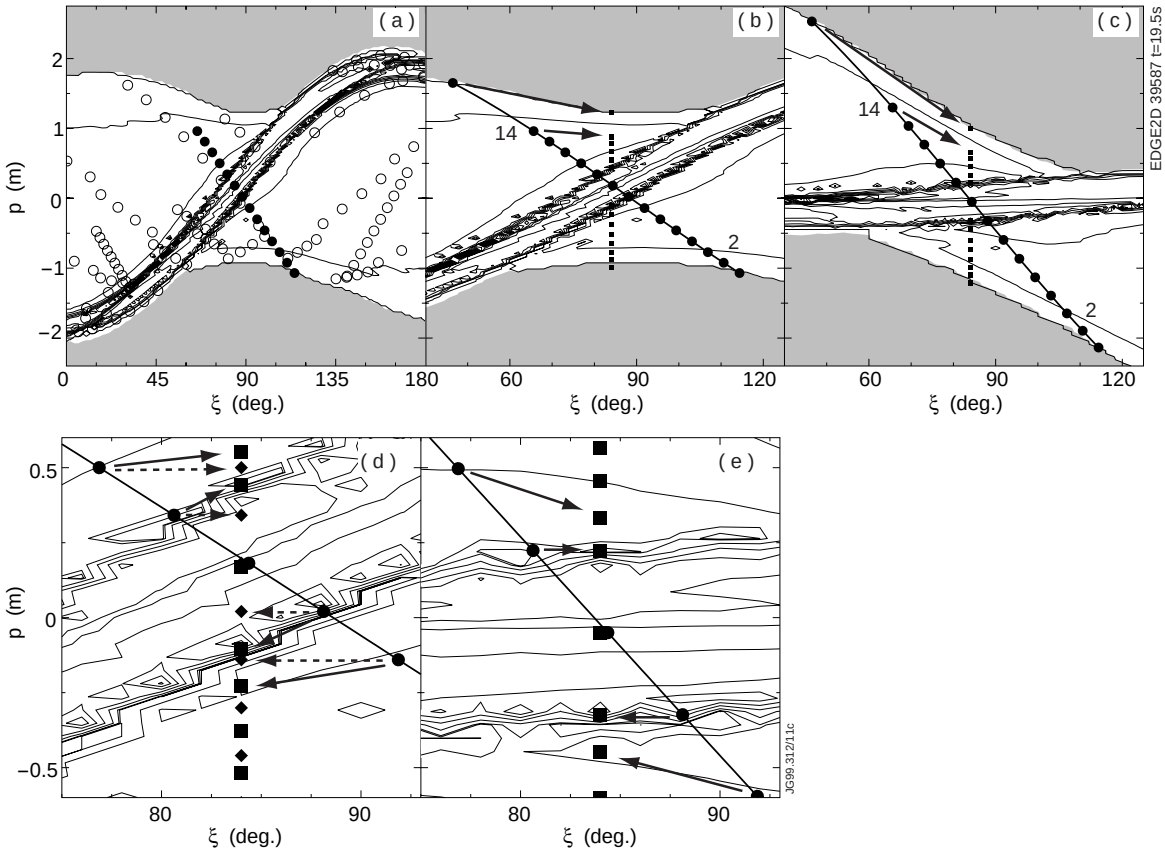

Fig.3: Contour plots of the sinogram for the simulated attached plasma [Fig. 2(a)]. The gray area is the area of projection space where lines of sight do not pass inside the JET vessel. (a,b,d) Origin of projection space on nominal magnetic axis. (c,e) Origin of projection space in X point. (a) Solid circles: average lines of sight of the KB1 vertical camera; open circles: average lines of sight of the other bolometer channels. (b,c) Blow up of (a); curve: aperture curve of the KB1 vertical camera; solid circles: channels of KB1 vertical camera plus a virtual (zero) channel just outside the boundary; solid squares: lines of sight projected onto the line $\xi = 84^\circ$ *with scaled* p. *(d,e) Blow up of (b,c); solid diamonds: lines of sight projected onto the line* $\xi = 84^\circ$ *with* unscaled p. *The solid arrows in (b,c,d,e) show the projection process onto* $\xi = 84^\circ$ *with scaled* p *for some lines of sight. The dashed arrows in (d) show the projection process onto* $\xi = 84^\circ$ *with* unscaled p. *The contours of the plots are not equidistant to enhance lower values (of the bulk plasma). The ragged shape of the contours is due to the coarseness of the* (p, ξ) *grid used.*

3.2 Weights determined from the sinogram

The $\xi = \text{const}$ line chosen in the following is $\xi = 84°$, which is centered on the KB1V line of sight viewing the center of the divertor. This seems slightly more appropriate than $\xi = 90°$, but one loses the benefit of the more exact calculation of the first equality in Eq. (5). The simplest method to map the aperture curve to a $\xi = \text{const}$ line is to keep the p constant (unscaled p), and just change the ξ to $\xi = \text{const}$. Figure 4 shows the cross-section of the sinogram of Fig. 3 at $\xi = 84°$ (solid curve) and the projection of the sinogram values along the aperture curve to $\xi = 84°$ with unscaled p (dotted curve). For $p < -0.5$ and $p > 1.0$ it is clear that due to the elongated shape of the plasma the sinogram is "squeezed" around $\xi = 90°$, and therefore it is appropriate to apply this squeezing in the mapping [arrows in Fig. 3(b)], which results in a scaled p. Close to the X-point the scaling in this way is very slight [diamonds and dashed arrows

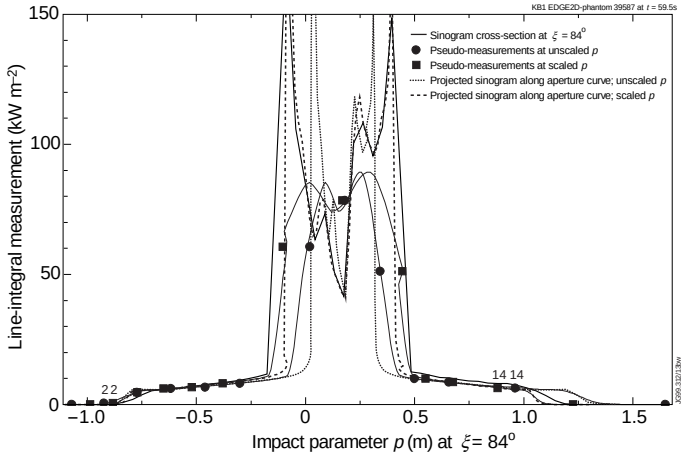

Fig.4: Cross-section of the sinogram (solid black curve), projected sinogram curves (dotted and dashed) and projected measurements (points connected by thin lines), all at $\xi = 84°$. *The circles and the dotted curve are projected with unscaled* p, *whereas the squares and the dashed curve are projected with scaled* p. *The thin curves through the points are the convolutions of the dotted or dashed curves, respectively, with the normalized nominal angular étendue of the system (instrument function, see Sec. 4).*

in Fig. 3(d)]. This mapping is satisfactory for the bulk plasma, for example in the limiter phase of a discharge. However, from Fig. 3(d) and the dotted curve in Fig. 4 it is evident that this mapping is unsatisfactory at the X point: the extent of the X-point radiation is underestimated, which would lead to too low a total radiation. An improved mapping is indicated by the solid arrows in Fig. 3(d). A convenient way to formulate this mapping is in projection space of which the origin lies in the divertor or X point [Figs. 3(c) and 3(e)]: in these coordinates (p', ξ') the three central channels are mapped with unscaled p', whereas the other channels are squeezed proportionally to their distance from $\xi = 84°$. This leads to the improved mapping of the dashed curve in Fig. 4. The effect on the measurements (including the beam widths) is given by the squares with respect to the circles. The total radiated power values obtained with weighted summation with unscaled and scaled p are given in Table I. As expected, the values obtained with unscaled p are far too low, while the values obtained with scaled p are very reasonable.

Table I *Total radiated powers determined in different ways from the emission profiles in Figs. 2 and 4.*

Method	**Total radiated power (MW)**
Simulated emission profile	1.12
KB1-only tomographic reconstruction	1.14
Tomography with all channels	1.03
Weighted summation, unscaled p	0.88
Weighted summation, scaled p	1.06

It is remarkable that although the three central lines of sight of the vertical KB1 camera seem virtually parallel in the divertor, the fan-shape distribution has a major impact on the scaling of p that has to be applied in the mapping from the aperture curve to $\xi = \text{const}$. Not the peakedness of the divertor radiation is the problem, but the divergence of the lines of sight. Therefore, it can be concluded that the calculated total radiated power will not depend strongly on the peakedness of the divertor radiation, but rather on the broadness and on the ratio of divertor to bulk radiation. Because the sinogram is given by the line integrals, it mixes bulk radiation (which requires a squeezed mapping of p) with divertor radiation (which requires an expanded mapping of p close to the X point). It is clear that it may be difficult to find a single set of weights Δp_i in Eq. (6) that gives satisfactory results for widely different plasmas, as will become clear from the following.

3.3 Comparison of weighed summation and tomography

Figure 5 shows the total radiated power calculated by a number of methods as a function of time for an L-mode density-limit discharge. It is clear that in this plasma, in particular after $t = 17\text{s}$ when the neutral-beam heating is switched on, the weighted summation with unscaled p the estimated radiated power is lower than the more reliable estimates by up to 30%, which is even worse than for the simulated data in Table I. The weighted summation with scaled p is also lower than the more reliable values form tomography. The two tomography methods (with all available channels and with KB1 only) agree very well. It should be said that this is a case with an exceptionally large discrepancy between methods; for a wide range of plasma parameters it has been found that the discrepancy is about 10% of the value. It is often found that the tomography method with all channels give abnormally high values for the radiated power when compared with the KB1 reconstructions; this is likely to be caused by artefacts introduced as a result of inconsistencies in the measurements. These results are further evidence that it is impossible to find one set of weights Δp_i in Eq. (6) that gives satisfactory results for widely different plasmas and also show that the determination of the total radiated power is far from trivial.

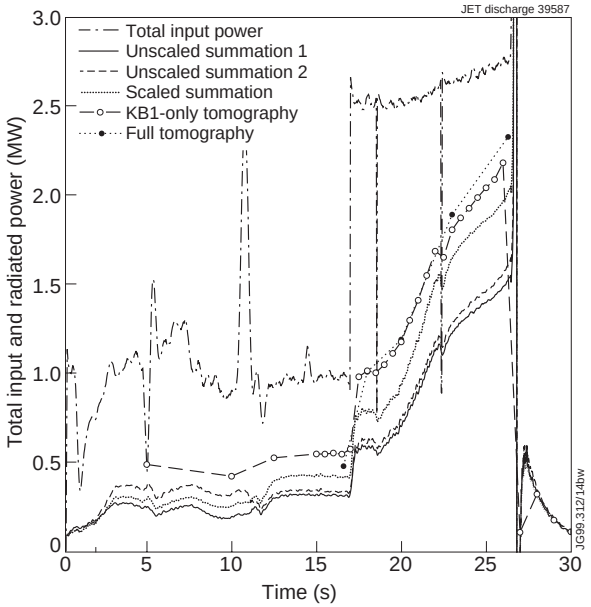

Fig.5: Total radiated power calculated by the various methods for an L-mode density-limit discharge in the JET MkIIA divertor [incidentally, the same discharge that was simulated in Fig. 2(a)]. Two different sets of weight with unscaled p *were used; 1: elongation in limiter phase ($t < 12$ s) taken into account; 2: fixed weights as obtained from Fig. 3 in the divertor phase (not shown in limiter phase). The total input power is shown for comparison only; a stable plasma cannot radiate more power than the input power.*

3.4 Other ways of finding weights

Given the finding that the tomographic reconstructions give reliable values for the total radiated power (Sec. 2), it is possible to find weights of the summation by fitting the weights so that the sum gives the total radiation known from tomography. Statistical methods can be used to find appropriate weights for a wide range of discharges. Such a method has been applied at ASDEX-U.[10] Also, a neural network could be trained for this purpose. To successfully apply such statistical methods, a large database with reliable results for widely varying plasma parameters is required to find appropriate weights or to train the neural network. This has not been done at JET for lack of a sufficiently large database and because the above theoretical analysis shows that no set of weights can be found for the vertical camera that are suitable for a all plasmas, whatever method is used to find the weights. It may be possible, however, to find a more robust set of weights if lines of sight of the horizontal KB1 cameras are included.

4. EFFECTS OF BLURRING

In Fig. 4 the blurring, or smoothing, effect of the instrument function is evident. It is worthwhile to investigate the information loss due to the blurring and whether this can affect the total radiated power that is determined. It is convenient to do this investigation along the aperture curve.

The normalized angular étendues of the channels of the vertical KB1 camera are shown in Fig. 6(b). The angular étendues of all channels are similar; the reason for the variation in width and height is a cosine-effect due to the angle at which the various detectors view through the aperture. Because the instrument function of all channels can be assumed to be represented by

the one of one particular channel, $e(\xi)$, the blurring is given by the convolution of Eq. (2). Measurements at angles ξ_i are given by $\hat{f}_i = \hat{f}(p_{\mathrm{ap}}(\bar{\xi}_i), \bar{\xi}_i)$. Because $\int \bar{e}(\xi)\mathrm{d}\xi \approx 1$, it follows that

$$\int \hat{f}(p_{\mathrm{ap}}(\xi), \xi)\mathrm{d}\xi \approx \int f(p_{\mathrm{ap}}(\xi), \xi)\mathrm{d}\xi, \tag{7}$$

which means that no power is lost due to the blurring in a total power calculation along aperture curve. Note, however, that an uncertainty in the total power is introduced by the coarseness of the sampling and by the nonlinear scaling and mapping of Sec. 3.2.

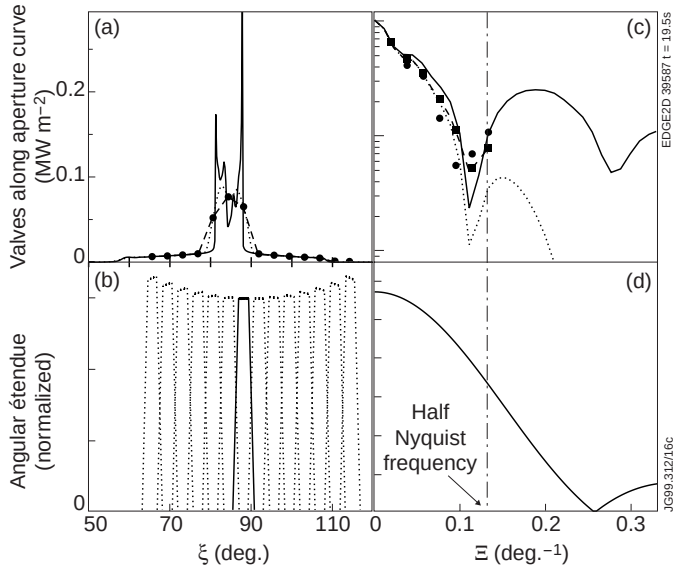

Fig.6: Quantities along aperture curve for the attached plasma of Fig. 2(a) as a function of the angle ξ (a,b) and its Fourier counterpart Ξ (c,d). (a) Sinogram values: solid line: line-integral values; dotted line: values blurred by instrument function; filled circles: points where the blurred values are sampled (corresponding to the detectors); dashed curve: piecewise-linear fit to sampled points. (b) Angular étendue (instrument function along aperture curve) normalized to the étendue for the vertical KB1 detectors; the one used in the investigation is given by the solid line. (c,d) Fourier transforms of (a) and (b), respectively, with equivalent linetypes and symbols. Note that (c) is on a logarithmic scale and (d) on a linear scale. Although the Fourier transforms were carried out with the discrete Fourier transform (DFT), the number of samples was chosen such that the figures are a good representation of the analytical Fourier transform, with the exception of the DFT of the discrete measurements (filled circles). The DFT of the discrete measurements is numerically inaccurate due to the small number of samples and the fact that the samples do not extend over the entire range of the plasma. The dashed curve in (c) indicates the blurred function aliased with values higher than half the Nyquist frequency [$(2\Delta\xi)^{-1}$, where $\Delta\xi$ is the sampling rate; vertical dot-dashed line at $\Xi = 0.13\ \mathrm{deg}^{-1}$]; the filled squares on this curve indicate the theoretical samples one would expect to find instead of the inaccurate filled circles.

Figure 6 shows the effect of blurring by the instrument function (angular étendue) for the sinogram values along the aperture curve. The Fourier transform of $\hat{f}$ along the aperture curve is given by

$$\hat{F}(\Xi) = \int \hat{f}(p_{\mathrm{ap}}(\xi), \xi)\, \exp(-2\pi i \xi \Xi)\, d\xi.$$

Although the variable ξ is periodic, and hence the corresponding frequency variable would be discrete, here the periodicity of ξ is irrelevant because the function that is Fourier transform goes to zero at both low and high ξ. Therefore, the frequency variable Ξ considered here is continuous. In Fourier space (for the coordinate along the aperture curve) the effect of the blurring and of the limited sampling by the detectors is very clear [Fig. 6(c)]. The values for $\Xi < 0.1\,\mathrm{deg}^{-1}$ correspond to the peak of radiation in the divertor, whereas peaks for $\Xi > 0.15\,\mathrm{deg}^{-1}$ correspond to the fine structure. In this example [the attached simulation of Fig. 2(a)] the peak at $\Xi \approx 0.2\,\mathrm{deg}^{-1}$ is not sufficiently damped by the instrument function [Fig. 6(d)] which leads to considerable aliasing. However, the amplitudes that are affected by the aliasing are relatively small, about a factor of 5 below the zero frequency component.

Noting that $\hat{F}(0)$ is equal to the "total" power along the aperture curve [Eq. (7)], it is clear that the zero frequency component carries the total power and that also in the Fourier domain the blurring (filtering at higher frequencies) has no effect on the total power if the signal is continuous. However, sparse sampling complicates the interpretation of $\hat{F}(0)$: due to aliasing $\hat{F}(0)$ may be incorrect. This is related to the observation in that integration over a piecewise linear fit to the measuring points of Fig. 6(a), i.e. a trapezoidal rule, may overestimate or underestimate the proper integral over the blurred curve. Because the regions where the piecewise linear fit is higher or lower than the blurred curve will largely cancel unless the sampling is extremely sparse with respect to the beam widths, the effect on $\hat{F}(0)$ will be small [as is also clear from the minimal aliasing at $\Xi = 0\,\mathrm{deg}^{-1}$ in Fig. 6(c)].

The instrument functions of neighboring channels overlap close to their half-maximum values [Fig. 6(b)]. This seems optimal as no emitting peaks between channels can be missed. However, the Fourier transform of the angular étendue has its first zero only at the Nyquist frequency $1/\Delta\xi$, where $\Delta\xi$ is the spatial sampling rate [see Fig. 6(d)]. Therefore, with this kind of limited overlap between instrument functions, significant aliasing can occur as discussed above [Fig. 6(c)].[11–13] The lobes of the Fourier transform of the angular étendue are so small that hardly any aliasing would occur if the overlap of the instrument functions were twice the current (i.e. the first zero of the Fourier transform of the angular étendue would coincide with half the Nyquist frequency). However, this would lead to a significantly reduced spatial resolution. Furthermore, Fig. 6(c) is an extreme case as in other cases the aliasing effect has been found to be much smaller. Therefore, the current overlap between the instrument functions appears to be a reasonable compromise between maximizing resolution and minimizing aliasing. However, one should always remember that aliasing can occur. Restoration or deblurring of the measurements is only possible if the sampling distance is much smaller than the beam widths.[13]

5. CONCLUSIONS

Calculating the total radiated power from properly regularized tomographic reconstructions is fairly reliable and is quite insensitive to most reconstruction parameters and the number of lines of sight used for the reconstructions, as long as the lines of sight used are consistent and contain a sufficient amount of information about the entire plasma cross-section. Unfortunately, at JET tomographic reconstructions are too time-consuming to be carried out for several time slices of each discharge, and should also be checked by hand.

A simpler and far more efficient calculation is possible by a weighted summation. The properties of such a weighted summation were studied in a fundamental way in projection space and for actual measurements. The results for the JET bolometer system are thought also to be valid for similar weights determined in other ways, for example by statistical methods. It was found that the weights of the weighted summation depend on the profile shape of the emissivity, in particular on the divertor radiation, and it does not seem to be possible to obtain a robust set of weights that gives accurate total radiated powers for widely different plasmas. The limitations to the method seem to stem from the combination of a local peak of radiation in the divertor and the fan-distribution of the lines of sight (the total radiated power determined from truly parallel lines of sight should not suffer from these problems). However, it should be possible to find suitable sets of weight for classes of similar discharges. To establish such sets many time-consuming tomographic reconstructions would be necessary for each class as a reference.

Beam widths of the measuring system (the instrument function) do not significantly affect the total radiated power determined by a weighted summation. One should, however, be aware of the danger of aliasing if the distance between lines of sight is not considerably smaller than the beam widths.

ACKNOWLEDGMENTS

The author is grateful to Dr. C.F. Maggi for the EDGE2D/NIMBUS simulations that gave the simulated emission profile of Fig. 2(a), to Dr. J.C. Fuchs for discussions on methods to determine the total radiated power, and to Dr. G. Por for discussions on Fourier analysis.

[1] E.R. Müller and F. Mast, “A new metal resistor bolometer for measuring vacuum ultraviolet and soft x radiation,” J. Appl. Phys. **55**, 2635–2641 (1984)

[2] K.F. Mast and H. Krause, “Bolometric diagnostics in JET,” Rev. Sci. Instrum. **56**, 969–971 (1985)

[3] K.F. Mast *et al.*, “A low noise highly integrated bolometer array for absolute measurement of VUV and soft x radiation,” Rev. Sci. Instrum. **62**, 744–750 (1991)

[4] R. Reichle *et al.*, “Bolometer for ITER,” in *Diagnostics for Experimental Thermonuclear Fusion Reactors*, eds. P.E. Stott *et al.*, (Plenum Press, New York, 1996), pp. 559–570

[5] L.C. Ingesson *et al.*, "Radiation distribution and neutral-particle loss in the JET MkI and MkIIA divertors," in *Proceedings of the 24th EPS Conference on Controlled Fusion and Plasma Physics (Berchtesgaden)*, Ed. M. Schittenhelm *et al.*, Europhysics Conference Abstracts Vol. 21A (EPS, 1997), Part I, pp. 113–116

[6] L.C. Ingesson *et al.*, "Radiation distribution and neutral-particle loss during detachment in JET," in *Proceedings of the 26th EPS Conference on Controlled Fusion and Plasma Physics (Maastricht)*, Europhysics Conference Abstracts Vol. 23J (EPS, 1999), pp. 257–260

[7] L.C. Ingesson *et al.*, "Soft x ray tomography during ELMs and impurity injection in JET," Nucl. Fusion **38**, 1675–1694 (1998)

[8] L.C. Ingesson, "Comparison of methods to determine the total radiated power in JET", to appear as JET report JET–R(99)06 (JET Joint Undertaking, Abingdon, UK, 1999)

[9] L.C. Ingesson *et al.*, "Projection-space methods to take into account finite beam-width effects in two-dimensional tomography algorithms," J. Opt. Soc. Am. A **16**, 17–27 (1999)

[10] M. Maraschek *et al.*, "Real-time determination of total radiated power by bolometric cameras with statistical methods," Rev. Sci. Instrum. **69**, 109–115 (1998)

[11] A. Macovski, "Physical problems of computerized tomography," Proc. IEEE 71, 373–378 (1983)

[12] A.G. Lindgren and P.A. Rattey, "The inverse discrete Radon transform with applications to tomographic imaging using projection data," Advances in Electronics and Electron Physics **56**, 359–410 (1981)

[13] R.N. Bracewell, "Correction for collimator width (restoration) in reconstructive x-ray tomography," J. Computer Assisted Tomography **1**, 6–15 (1977)